

Offset-Free Magnetic Field Sensor Based on a Standing Spin Wave

Markus Gattringer^{1,*}, Claas Abert¹, Qi Wang², Andrii Chumak², and Dieter Suess¹

¹*Physics of Functional Materials, Faculty of Physics, University of Vienna, Kolingasse 14–16, 1090 Vienna, Austria*

²*Nanomagnetism and Magnonics, Faculty of Physics, University of Vienna, Boltzmannngasse 5, 1090 Vienna, Austria*

 (Received 17 April 2023; revised 28 July 2023; accepted 6 October 2023; published 31 October 2023)

Magnetic field sensors are used intensively in many areas of our lives and the demands on their properties are constantly growing. One of the biggest challenges is the development of an offset-free sensor that provides a zero signal at zero field, regardless of the manufacturing accuracy. Here, we propose the concept of an offset-free sensor, based on the use of standing spin waves. The dispersion of the spin waves strongly depends on the applied magnetic field, so that the excitation maximum of the standing wave shifts with the change of the field. Spin pumping in combination with the inverse spin Hall effect is used to detect the sensor signal directly, in the form of a dc voltage. The offset-free functionality is achieved by reversing the magnetization direction of the spin-wave waveguide. The functionality of the sensors is proven numerically and concepts for practical implementation are presented.

DOI: [10.1103/PhysRevApplied.20.044083](https://doi.org/10.1103/PhysRevApplied.20.044083)

I. INTRODUCTION

Magnetic field sensors have become a part of our everyday lives. In addition to simply measuring a magnetic field, they are also used to detect motion (both linear and circular) via the change of a magnetic bias. Elaborate detection schemes include superconducting quantum interference devices (SQUIDs) [1] and nitrogen-vacancy (N-V) detectors [2], while variants of Hall-effect sensors [3,4] and magnetic tunnel junctions (MTJs) [5–7] (based on tunnel magnetoresistance (TMR) [8]) are used in large numbers in automation, the automotive sector, and aviation.

The transfer curve, the signal S produced by a magnetic field sensor, is a function of the measured field H . But there generally exists a nonzero offset O , such that even when $H = 0$, a signal will still be detected. This offset is either a result of the operational concept of a sensor and the underlying physics or it originates from engineering constraints [4]. For a TMR measurement, the resistance of the MTJ is measured, which is of course nonzero. For Hall-effect sensors, the generated Hall voltage is in principle free from offset but fabrication errors and material defects introduce a measured output voltage.

To eliminate the offset, different methods are employed. For MTJs, an array of four detectors is connected in a Wheatstone-bridge setup to nullify the measured resistance in the zero-field case [9,10]. For Hall-effect sensors, a so-called spinning-current setup is used, whereby different contacts of the Hall cross have voltage applied to them successively; the offset can then be nullified by comparing the different resulting signals [11]. In both cases, offset elimination results from the comparison of different signals. The elimination can therefore only be complete if all those subsignals behave perfectly identically. In practice, a finite offset remains, due to fluctuating material parameters, fabrication errors, and temperature fluctuations (thus making the offset temperature dependent [12]). Contemporary MTJ-type sensors exhibit offsets of several millitesla even after the nullification setup [13,14].

Here, we propose an alternative sensor design: a *standing spin wave* in a waveguide, with a fixed frequency and wavelength. This probes a fixed point in dispersion phase space, with the excitation efficiency changing as a function of the external field. The uniaxial shape anisotropy is exploited to create two different magnetization configurations and therefore two different modes of precession (clockwise and counterclockwise, with respect to a fixed coordinate system). Employing spin pumping [15] and the inverse spin Hall effect [16] as means of detection, this results in opposite signals of identical magnitude for no measured quantity—such that the output cancels itself out—and an offset-free transfer curve. Conceptually, this follows the idea of the spinning current, using successive

*markus.gattringer@univie.ac.at

Published by the American Physical Society under the terms of the [Creative Commons Attribution 4.0 International](https://creativecommons.org/licenses/by/4.0/) license. Further distribution of this work must maintain attribution to the author(s) and the published article's title, journal citation, and DOI.

comparative measurements. The different measurements here always employ the very same parts of the system, and not different current paths and leads as for the spinning current, thereby eliminating possible sources of offset. With that said, for a real device, the necessary complete reversal of the magnetization is a major challenge.

It should be noted here that several works about magnon-based sensing of magnetic fields have already been published. Spin waves are very sensitive to an external field and various methods can be proposed to develop magnonic sensors. In the simplest case, similarly to this work, a change in the external magnetic field shifts the spin-wave dispersion curve, resulting in a different wavelength but a conserved frequency [17]. Another way of constructing highly sensitive devices is to employ periodic magnonic structures—magnonic crystals [18–20]. Generally speaking, all the advantages inherent in the field of magnonics (see recent road maps [21,22]) can also be used for the development of sensors: scalability to lateral sizes below 100 nm; the wide range of parameters to tune the sensor characteristics (choice of the material, size, and shape of the structures, crystallographic anisotropy, etc.); nanosecond-order dynamic reconfigurability; low energy consumption; the ability to construct periodic magnonic crystals; the ability to operate in three-dimensional (3D) nanostructures for the development of 3D field sensors; and compatibility with a variety of spintronic and CMOS electronic devices. This enables the development of sensors with specific functionalities and/or parameters.

The general interest seems to be in constructing a highly sensitive sensor (hence employing magnonic crystals), whereas we aim for a simple offset-free design. Precession-type sensors have also been presented before, as spin-torque oscillators, which are structurally similar to

MTJs but instead employ giant magnetoresistance (GMR) [23,24]. Also, spintronic effects are commonly used for proposed sensors but this is limited to spin-transfer torque (STT) or spin-orbit torque (SOT, based on forward spin Hall effect), i.e., direct injection of spins [23–25]. Spin pumping has never been proposed as part of a practical sensor, although it is commonly used as a detection method in experimental magnonics [26–28].

II. SYSTEM DESCRIPTION AND MODE OF OPERATION

The structure of the sensor is shown in Fig. 1. A waveguide, made out of yttrium iron garnet (YIG, $\text{Y}_3\text{Fe}_5\text{O}_{12}$), with a cross section of 50×50 nm, forms the base. The cross section is square to minimize shape effects (i.e., elliptic precession). It is magnetized longitudinally, i.e., $M_{\parallel}/M_S = m_x = \pm 1$, where \mathbf{M} is the local magnetization and M_S is the saturation magnetization. Atop of it, platinum strip lines with width w and height $h = 15$ nm are placed at an interline distance $d = 2w$. By applying an alternating current \mathbf{j}^{ac} with a frequency f to the strip lines, where the phase of the current is shifted by $+\pi$ between neighboring strip lines, a standing spin wave with $\lambda = d$ will be excited in the waveguide due to the Oersted fields generated by the currents. We use $\|\mathbf{j}^{\text{ac}}\| = 2 \times 10^{11}$ Am² here.

The choice of f^{ac} and λ is described in Sec. III; for our computations, we use $f = 3.3$ GHz and $\lambda = 180$ nm. The wavelength will be locked in, determined by w and d . The sensor therefore probes a fixed point in the dispersion phase space [Fig. 2(a)].

It is instructive to examine this phase space more closely. From Fig. 3, we can estimate that the device

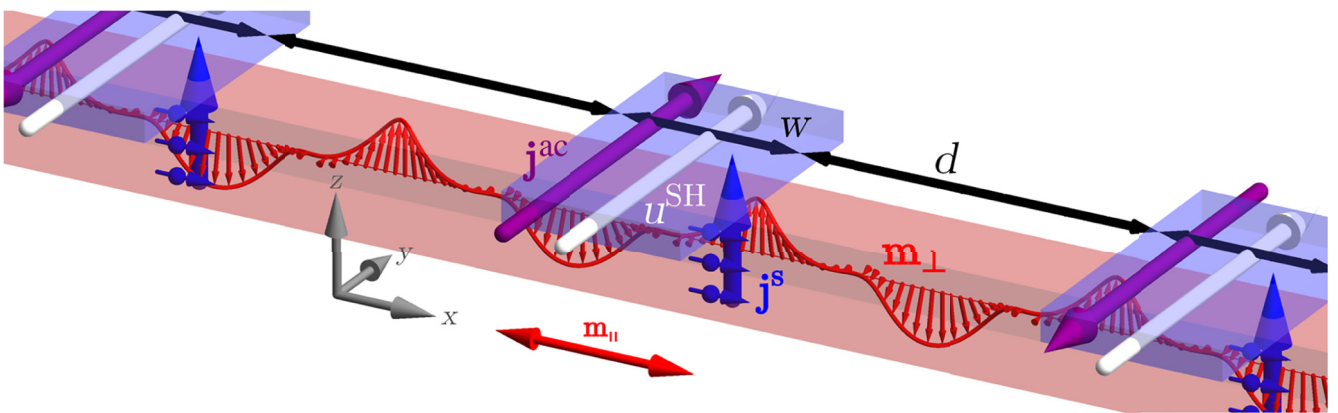


FIG. 1. A schematic of the sensor structure. The YIG waveguide is in light red and the Pt strip lines are in light blue. $\lambda = d = 2w = 180$ nm. A standing spin wave (red, where the transversal component of the magnetization, \mathbf{m}_{\perp} , relative to the waveguide center, is depicted for an arbitrary time) is excited in the waveguide by the Oersted field of an applied (purple) alternating current \mathbf{j}^{ac} . The precessional motion of the wave generates a (blue) spin direct current $\hat{\mathbf{j}}^{\text{s}}$ via spin pumping. The spin Hall effect in the strip line converts this into a charge direct current \mathbf{j}^{SH} , resulting in a (white) measurable voltage u^{SH} . The longitudinal component of the magnetization \mathbf{m}_{\parallel} is pointed along the x axis.

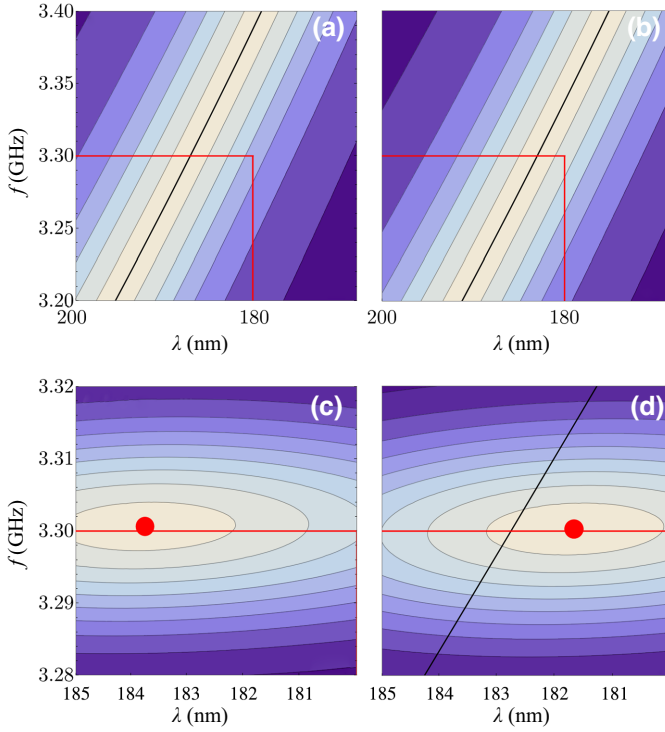


FIG. 2. An idealized schematic of the working principle and wavelength change of the sensor. Intensity contour plots are shown, with light colors for high intensity. (a),(c) Applied field along the $+x$ axis. (b),(d) Applied field along the $-x$ axis. The thick black line marks the maximum of the dispersion relation. (a),(b) The dispersion relation, with the probing point marked. The dispersion relation gets (“vertically”) shifted by field changes and the probing point lies at a different intensity, producing a different signal. (c) [corresponding to (a)] and (d) [corresponding to (b)] Detailed views of the product of the dispersion-relation susceptibility and the excitation distribution of the antenna array. This product is shifted toward the maximum of the dispersion relation and hence the resulting wave will always have higher λ and f in the operational regime.

operates in an exchange-dominated region. The magnetic susceptibility, and hence the shape of the dispersion relation, is then approximately given by (see, e.g., Ref. [29, Chap. 7])

$$\hat{\chi} = \frac{\omega_M}{(\omega_k + \omega_B - 2\pi f)^2 + (2\pi\alpha f)^2} \begin{pmatrix} \omega_k + \omega_B - 2\pi f & 2\pi\alpha f \\ -2\pi\alpha f & \omega_k + \omega_B - 2\pi f \end{pmatrix}, \quad (1)$$

where $\omega_M = \gamma_e \mu_0 M_S$, $\omega_B = \gamma_e (B_{es} + \mu_0 H_x)$, and $\omega_k = 8\pi^2 \gamma_e A / M_S \lambda^2$. γ_e is the gyromagnetic ratio and μ_0 is the magnetic constant; M_S , A , and α are listed in Table I; B_{es} is the effective shape anisotropy field of the waveguide (i.e., the field keeping the magnetization longitudinally aligned) and H_x is the external field; both are assumed to

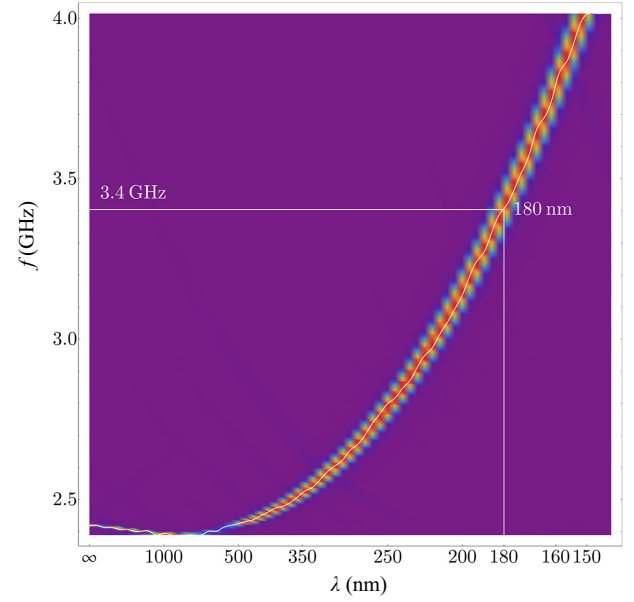


FIG. 3. The magnon dispersion relation for a longitudinally magnetized YIG waveguide of 50×50 nm cross section. An interpolated approximation (white) has been overlaid on the color map. The magnon exhibits backward-volume magneto-static behavior. The white cross lines denote the position at $\lambda = 180$ nm and approximately $f = 3.4$ GHz.

be exclusively in the x direction. Note that this is a real susceptibility. This introduces the first operational limit on the setup: the derivation is only valid for small amplitudes and hence the device is restricted to small Oersted fields. The observed angle of precession is 3° , which is still within that limit, at least for a nanoscale waveguide. The second operational limit is immediately visible: the susceptibility is not linearly dependent on ω_B (i.e., H_x) and so the sensor response is only approximately linear for small external fields. The shape of the off-diagonal components of the susceptibility is that of a Lorentz distribution. In this linear case, the amplitude of the wave follows from

$$\mathbf{M} = \hat{\chi} \cdot \mathbf{H}_{Oe}, \quad (2)$$

where the M_x component is set at M_S for small excitations and \mathbf{H}_{Oe} is the harmonic Oersted field in the y - z plane. The rate of precession can be obtained from this term by differentiation of the harmonic field with respect to time, such that

$$\frac{d\mathbf{M}}{dt} = \hat{\chi} \cdot \frac{d\mathbf{H}_{Oe}}{dt}. \quad (3)$$

The application of an external field [going from Fig. 2(a) to Fig. 2(b)] along the waveguide (i.e., H_x) will shift the dispersion relation in the frequency direction, thereby sweeping it along the probing point. The amplitude and rate of precession of the excited standing wave therefore

TABLE I. The material parameters used.

Waveguide			
Gilbert damping	α	2×10^{-4}	
Waveguide and interaction layer			
Saturation magnetization	M_S	1.4×10^5	A m^{-1}
Exchange coupling	A	3.6×10^{-12}	J m^{-1}
Interaction layer			
Gilbert damping	α	1×10^{-2}	
Electronic coupling	J	1.32×10^{-20}	J
Strip lines and interaction layer			
Electronic diffusion constant	D_0	5×10^{-3}	$\text{m}^2 \text{s}^{-1}$
Conductivity	C_0	4.5×10^6	S m^{-1}
Spin-flip time	τ_{sf}	8×10^{-15}	s
Spin Hall angle	Θ_{SH}	0.1	

change as a function of external field, acting as a measured quantity.

In principle, the wavelength of the standing wave should not change during operation. Realistically, however, the standing wave will not be perfectly monochromatic. Hence the probing point should be considered as a two-dimensional distribution in phase space, with the distribution acting as weights for the dispersion relation. The result is a product of both, and the antennas will excite wavelengths that are not λ , as intended, but slightly larger [Figs. 2(c) and 2(d)]. Due to the shape of the dispersion-relation susceptibility, this shift becomes larger the further away the sensor is from the maximum of the relation. The observed wavelength in computation indeed always stays 1–5 nm above $\lambda = d$.

The major advantage of using a standing wave, compared to homogeneous precession [in effect, a ferromagnetic resonance (FMR) setup], originates from more precise excitation. For a standing wave, the excitation can be easily achieved via strip-line antennas. For homogeneous precession in a microstrip, unwanted standing-wave contributions will always emerge [30], polluting the sensor response.

Spin pumping creates a spin accumulation \mathbf{s} at the YIG-Pt boundary. Here, direct approximations are only possible for homogeneous precession, as cross-diffusion processes (see Sec. III B), which no longer allow an analytical solution, have to be considered. Still, we reproduce Eq. (15) from Ref. [31]:

$$\mathbf{s}(z) = -\frac{\Gamma_{IS} \chi_e}{1 + \Gamma_{IS}^2} \frac{\hbar (1 + \alpha^2)}{J (1 + \alpha^2 + \chi_e)} \cosh\left(\frac{h-z}{\lambda_{\text{sf}}}\right) \times \text{sech}\left(\frac{h}{\lambda_{\text{sf}}}\right) \left(\frac{\partial \mathbf{M}}{\partial t} + \frac{\Gamma_{IS}}{M_S} \mathbf{M} \times \frac{\partial \mathbf{M}}{\partial t}\right). \quad (4)$$

For χ_e and Γ_{IS} , see the definitions in the cited source; both are combinations of material and system parameters listed in Table I. \hbar is Planck's reduced constant and

$\lambda_{\text{sf}} = \sqrt{2D_0\tau_{\text{sf}}}$ is the spin-flip length; D_0 and τ_{sf} are listed in Table I. From Sec. III C of Ref. [31], we estimate the effect of the cross diffusion as follows. As one strip line covers, in principle, exactly half a wavelength, the distribution of spin accumulation along the waveguide below the strip line should follow the behavior of a standing wave. Since we are interested in its x component, we simply treat it as $\propto \sin(2\pi x/\lambda)$ and average over half a wavelength. This yields a prefactor $2/\pi$ or a simple proportionality. This is not strictly correct but it should hold for the small-amplitude approximation used as our starting point. This spin accumulation creates a spin direct current $\hat{\mathbf{j}}^{\text{s}}$ into the strip lines, with a spin direction that is parallel to the waveguide (i.e., j_{xz}^{s}). [It also creates a spin alternating current with an orthogonal spin direction (i.e., j_{yz}^{s}) but this is not important for our considerations.] This spin direct current is then transformed into a charge direct current parallel to the applied alternating current by the inverse spin Hall effect (SHE) [16],

$$j_y^{\text{SH}} = 2 \frac{e}{\mu_B} D_0 \Theta_{\text{SH}} \frac{\partial s_x}{\partial z}. \quad (5)$$

Averaging over the current for the total height of the strip line removes the coordinate dependence. Assuming a long enough strip line (which is true in practice), boundary effects can be ignored for analytical purposes and a simple Ohmian approximation made for the voltage u^{SH} that results from this current. Note that the high frequencies involved will render this approximation invalid for the oscillatory components but it is valid for the stationary one. Also, the spin drift-diffusion model is formulated using Ohm's law, such that the analytical model and the numerics agree.

From the presented equations and arguments, the expected voltage can be approximated and, more importantly, the response

$$\frac{\partial u^{\text{SH}}}{\partial H_x} \propto \frac{2\pi f (\omega_k + \omega_B - 2\pi f)}{((\omega_k + \omega_B - 2\pi f)^2 + (2\pi \alpha f)^2)^2}, \quad (6)$$

where all the amassed material constants and system parameters have been factored out. The signal, as could be expected, is roughly of square Lorentzian shape. Indeed, the fits in the plots shown herein have all been performed with a Lorentzian distribution, as that is still a good approximation of its square variant. The response is then of the classic shape of an FMR measurement. It is clearly not linear, as previously stated. This is only the case for small external fields. A quantifier for the linearity of magnetic field sensors has been introduced [32].

Even though the phase of \mathbf{j}^{ac} changes between neighboring strip lines, the sign of j_y^{SH} does not (as it is strictly dependent upon the direction of precession and hence on the axis of precession/initial magnetization direction).

Therefore, such a setup cannot be constructed as a meandering strip line, at least not unless special measures are taken. The setup that we use has been selected to keep computational effort down, as spin-pumping computation in a fully conducting waveguide (which may very well be the case for a practical application) is prohibitively costly. It still adequately demonstrates the physics and usability of the sensor.

For our setup, we use ten strip lines but this number can be increased, therefore amplifying the signal as needed. In principle, every strip line would produce the same voltage but this is not completely true for a finite-length waveguide due to symmetry reasons.

The sensor signal is then the sum of those of the individual strip lines, u^{SH} , by assuming a serial connection. As this is overlaid by u^{ac} , a suitable low-pass filter has to be applied to isolate it. It will be seen in the following that this filtering is also necessary for a second reason. To achieve an offset-free transfer curve S , we compare u^{SH} of the sensor for the magnetization of the waveguide in both directions along its longitudinal axis, i.e.,

$$S = u^{\text{SH}}(m_x = 1) + u^{\text{SH}}(m_x = -1). \quad (7)$$

Per the symmetry of the system, we expect two signals that have opposite sign for $H_x = 0$ (due to s_x having the opposite sign), with the signals being identical but shifted by $2 u^{\text{SH}}(H_x = 0)$. Consequentially, the response is

$$\frac{\partial S^{\text{SH}}}{\partial H_x} = 2 \frac{\partial u^{\text{SH}}}{\partial H_x}. \quad (8)$$

Such an additive measurement then enables us to generate an offset-free transfer curve from a single device, with all possible deviations (fabrication and material parameters) being nullified by the symmetry. In practice, the magnetization of the sensor would need to be periodically (on a millisecond scale) inverted by short application of an external field to enable this differential measurement.

III. SIMULATION RESULTS

To perform simulations, we use our finite-element-based micromagnetics solver suite MAGNUM.PI, an evolution of the earlier MAGNUM.FE [33]

We have recently developed a spin-pumping add-on [31], which we are using to compute the spin pumping and the inverse SHE. This is the first setup that can handle spintronics entirely self-consistently and has been specifically developed for such tasks. Spin-pumping effects are only computed after the standing wave has properly formed (after 400 excitation cycles) and then only the generated spin current, but not the feedback effects due to spin torque. While a fully self-consistent computation is possible, the already long computation times would explode doing so.

To facilitate the computation of spin pumping in this way, an interaction layer has to be defined where the s - d coupling (between the s electrons of the strip line and the d electrons of the waveguide) is active. The layer is located in the waveguide, directly underneath each strip line, with a thickness of 1 nm. This also includes an overhang to both sides of the strip line of 1 nm. For the purpose of the simulation, this interaction layer has the properties of both the waveguide and the strip line. To account for the fact that we do not compute fully self-consistently, we approximate the spin torque, and the change of local damping, by increasing the Gilbert damping in the interaction layer from 2×10^{-4} to 1×10^{-2} . This is a reasonable approximation; both the experimental results (with a bulk increase in YIG-Pt systems by a factor of 5 [34]) and our results in Ref. [31] suggest an increase around the order of 250 for the interaction layer. It has to be noted here that an interaction layer of 1 nm is not realistic; the s - d interaction is likely limited to a single atomic Pt layer; hence a value of 0.2 nm would be more sensible. Since such a thin layer is numerically challenging to handle, we settle for the larger value. This means that the voltages presented herein faithfully capture the qualitative behavior of the device but are most likely an order of magnitude higher than what would be measured in experiment. The modified Gilbert damping is reduced by a factor of 5 to account for the large interaction layer thickness; hence we arrive at 1×10^{-2} .

The total waveguide length is $7.32 \mu\text{m}$, with the strip-line battery of size $14\lambda = 2.52 \mu\text{m}$ centrally located. The outermost $2 \mu\text{m}$ of both ends of the waveguide have increasing Gilbert damping (parabolic trajectory) to suppress the outgoing magnon while reducing reflections. The wave is only standing in the center of the system and starts to have a propagating character further away from it, resulting from asymmetry. A longer waveguide and/or reflecting boundaries should be able to suppress that propagation.

The material parameters that were used are listed in Table I. The spin diffusion, demagnetization, magnetic exchange, and Oersted field of the strip lines are computed.

To find a suitable probing point, we first compute a dispersion relation and a voltage spectrum for the system.

A. Dispersion relation

To compute the dispersion relation, we use the method described in Ref. [35]. The result is shown in Fig. 3. The relation does not take antenna geometry into consideration. It exhibits backward-volume magnetostatic behavior for large wavelengths; the sensor is already operating in the parabolic exchange regime.

The value of λ selected for a real device would generally be determined by the position of an FMR. The wave number (and therefore λ) should be located at a suitable distance from the FMR condition (to enable a standing

wave to be properly formed) but preferably as close as possible to maximize excitation. We select $\lambda = d = 2w = 180$ nm and therefore $w = 90$ nm. This position is marked in Fig. 3 by the white cross lines.

B. Wave form

Figure 5(a) shows the signal (no filtering) for $f = 3.4$ GHz. Even though we naively expect constant voltage from spin pumping, there is a major oscillating contribution.

This can be understood in the following way. From Ref. [16], it follows that the spin-current component j_{xz}^s creates the charge-current component j_y^{SH} via inverse SHE. But by the simple mathematical definition (cross product), j_{zx}^s (exchanged indices) also creates j_y^{SH} . j_{zx}^s is a current along the waveguide, indicating a gradient of the spin-accumulation component s_z along the waveguide. This is illustrated in Fig. 4: due to the excitation, the standing wave always has a node at the center of the strip line, corresponding to small precession (in principle, even none) and, hence, little generated spin accumulation. At the edges of the strip line, the precession is markedly stronger but with opposite phase between the two edges. Thus the generated spin accumulation in the z direction is also opposite, forming said spin gradient. This relation will invert itself half a cycle later, creating an oscillating spin current j_{zx}^s and, hence, an oscillating contribution to j_y^{SH} . See also Ref. [31] for simple analytical formulas [especially Eq. (4)] for the generated spin accumulation.

Indeed, for any spin wave (standing or as a magnon), such an oscillating gradient always exists at any point of the waveguide. This effect is not noticed in experiments, however. This results from the large surface areas used to generate a measurable signal (see, e.g., Refs. [27,36]). In the presented sensor setup, where every strip line is centered around a node of the standing wave, with the detector width $\lambda/2$ (cf. Fig. 1), the oscillatory part is maximized. In experiments, the constant part is cumulative over the total surface area (usually many orders of magnitude larger than the spin-pumping area of our detection strips), while the oscillatory part is not. It is therefore reduced to almost unnoticeable noise in experiment.

A frequency spectrum of the signal is shown in Fig. 5(b). The dominant contributions, a constant signal originating from j_{xz}^s and an oscillation at 3.4 GHz from j_{zx}^s , can be easily seen. Aside from those, other modes, which result from spectral leakage, are also noticeable. It is therefore evident that a constant signal, and hence an offset-free response of the sensor, can only be achieved after a sufficiently long measurement time to generate a clean signal. With that said, again to keep computation times manageable, we limit signal processing to 50 cycles (approximately 15.2 ns). For further considerations, we apply a low-pass filter with cutoff at 800 MHz to the signal, to extract the

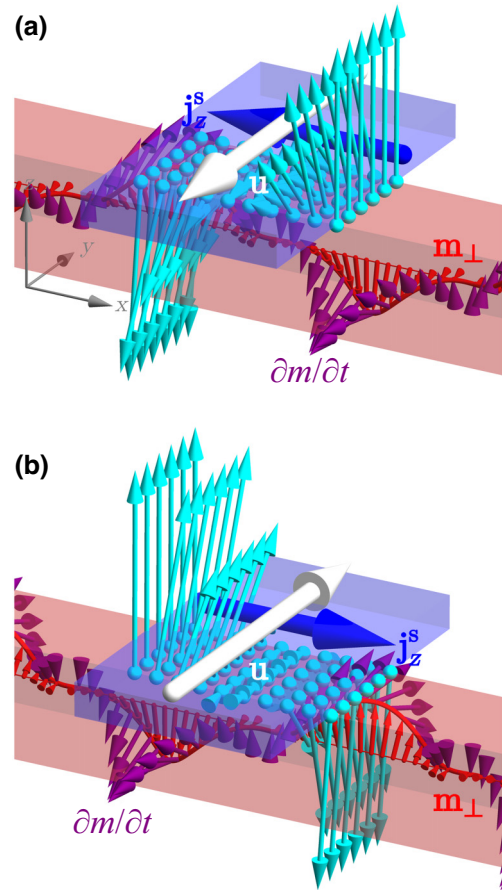


FIG. 4. The current of z spins \mathbf{j}_z^s , i.e., the z component of $\hat{\mathbf{j}}^s$, pumped by the standing wave. For any time, the standing wave (red) has a distinct phase angle and amplitude at any point along the waveguide, with a corresponding precession vector (purple arrows). The spin accumulation generated at the interface boundary (cyan spheres and arrows) then has varying direction and magnitude, creating a resulting spin current (blue) along the waveguide and a corresponding voltage. Parts (a) and (b) show states separated by half a cycle.

constant part. Only the central 10 ns of the result are then averaged, to drop the numerical artifacts introduced at the start and end of the signal due to the low-pass operation.

C. Frequency spectrum

We conduct a frequency sweep for the defined $\lambda = d = 2w$ to find the probing frequency. Figure 6(a) shows the spectrum of the sensor for $m_x = 1$. This can be understood as a slice through the dispersion relation, at λ , now also taking the antenna geometry into consideration. The FMR around 2.35 GHz is the dominant feature, whereas the small “line” of the standing wave is located around 3.4 GHz, as expected from the dispersion relation. The error bars near the FMR are considerable, thereby offering a justification for our earlier statement that the

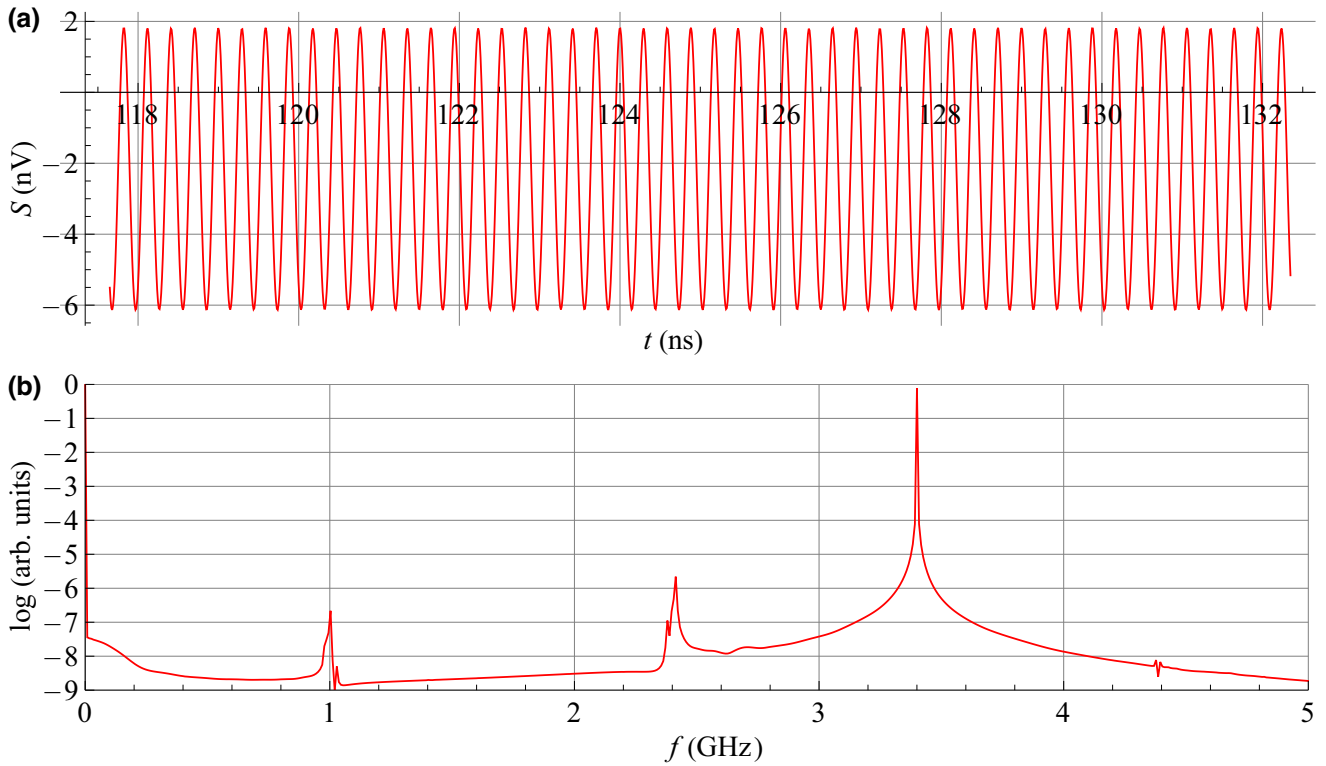


FIG. 5. (a) The inverse spin Hall signal at 3.4 GHz and $m_x = 1$ without an external field. The total signal is dominated by a constant shift and an oscillation at 3.4 GHz from excitation. (b) The frequency spectrum (Fourier transform) of the signal in (a). Other contributions, arising from spectral leakage, are also noticeable.

probing point should be sufficiently far away from the FMR.

Figure 6(b) shows the vicinity of the standing-wave peak but now the values (and corresponding Lorentz fits) of both magnetization orientations are plotted. The line width (full width at half maximum) is 188 nm. It is immediately noticeable that the signals are mirrored at the x axis, i.e., $u^{\text{SH}}(m_x = 1) = -u^{\text{SH}}(m_x = -1)$. Additive measurement of both configurations should therefore always provide an offset-free signal. We define the probing frequency of the sensor as 3.3 GHz, on the left slopes of the peaks.

D. Signal output

Figure 7 shows the output of the sensor as a function of the external field along the waveguide, i.e., H_x , the field to be measured. Figure 7(a) shows the two signals for $m_x = \pm 1$. Their behavior is identical; the only difference is the sign of the offset of the zero-field case, which corresponds to the sign of m_x . This is expected from Fig. 6(b). In Fig. 6(b) the two signals have been combined into the single transfer curve of the sensor as per Eq. (7). The signal is offset free within simulation accuracy; the numerical error amounts to an offset at 5 nT. We provide some insight into this matter in Appendix A.

E. Off-axis detection

Off-axis external fields (H_y and H_z) also have an effect on the generated signals. Naively, one can expect the axis of precession to be tilted away from the longitudinal axis of the waveguide. Hence the generated voltage should be different. Due to the symmetry, the transfer curve will again be offset free but the slope of the transfer curve should change. To test that assumption, we have repeated the computation from Sec. III D for an external field $\mathbf{B} = (H_x, H_x, H_x)^T$. We report here that the expected slope change was not identifiable in simulations, as it was below their numerical accuracy. We provide a short study of the contribution of the off-axis fields, and the numerical problems, in Appendix A. In any case, for the small fields for which the sensor would be usable, the effect will most likely be very low; this is especially true since a working design will most likely use a relatively long waveguide, with the resulting shape anisotropy providing a large resistance to precession tilt.

F. Fabrication errors

Since in Sec. I we have mentioned that fabrication errors are an obstacle to creating an offset-free sensor, it seems only reasonable to simulate fabrication errors. Numerical (and analytical) setups tend to be perfect; to move away

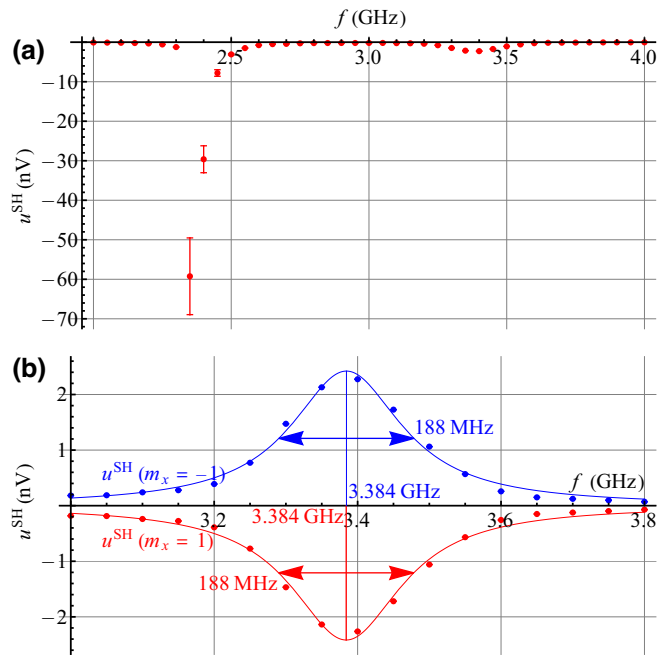


FIG. 6. (a) The signal spectrum of $u^{\text{SH}}(m_x = 1)$ (red) of the sensor. The values shown here are calculated as a 10-ns average of the 800-MHz low-pass-filtered signal. The error bars denote the standard deviation of this average. (b) A detailed view near the standing-wave peak: $u^{\text{SH}}(m_x = -1)$ in blue and $u^{\text{SH}}(m_x = 1)$ in red. The data points are computed values and the plotted lines are a fitted Lorentzian, with the parameters noted in the plot.

toward a more realistic case, we apply statistical deviations to the simulated system. Also, hysteresis effects from locally incomplete magnetization inversion can be approximated by this approach.

To simulate a system with fabrication errors, we have added an error term to the relevant system dimensions (the antenna sizes and positions). This was done by drawing from a normal distribution, with μ being the original dimension and $\sigma = 0.1\mu$. The resulting values are listed in Appendix B.

In addition, to simulate material defects, we have introduced a random field to the waveguide. This was done by drawing from a normal distribution, with $\mu = 0$ mT and $\sigma = 0.1$ mT for each vector component, at each vertex of the finite-element mesh. This resulted in a small, random, and fluctuating field within the waveguide.

The deviations introduced are intentionally very large to be able to discern any effects from numerical errors. A very obvious, and easily understandable, consequence of this process is that the amplitude of the generated standing wave is lower than for the optimal case. Deviations in antenna size and position mean that the single excitations no longer add up optimally. Figure 8 shows the signal output(s) and the resulting transfer curve for such a case.

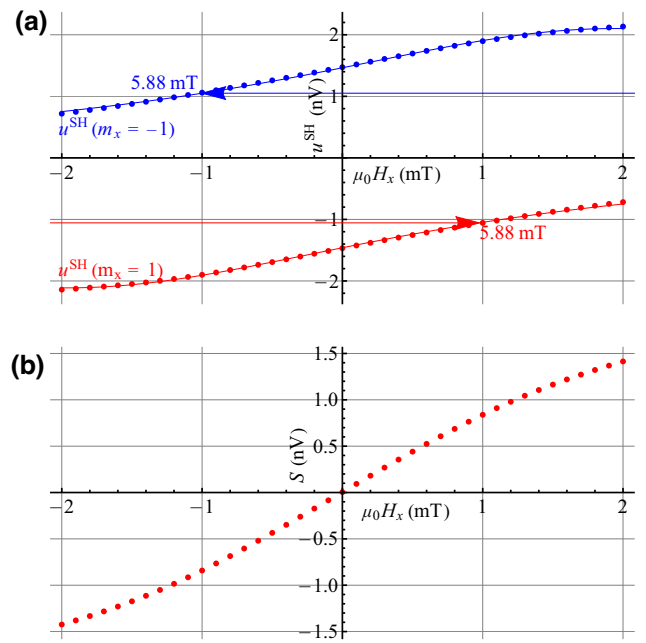


FIG. 7. (a) The sensor voltage signal as a function of the detected field at 3.3 GHz. The values shown here are calculated as an average over 10 ns of the low-pass-filtered $u^{\text{SH}}(m_x = 1)$ (red) and $u^{\text{SH}}(m_x = -1)$ (blue) with a cutoff at 800 MHz. The data points are computed values and the plotted lines are a fitted Lorentzian, with the line widths noted in the plot. (b) The sensor transfer curve obtained by adding the individual curves from (a) per Eq. (7).

Although the behavior is as expected, the signal magnitude drops to approximately half its original value. In contrast to the optimal configuration, it is no longer possible to attribute the remaining offset completely to numerical errors. Analysis of this is again provided in Appendix B. This is not unexpected: as the concept of the sensor relies on symmetry, the large deviations from that symmetry that have been introduced will invalidate the concept.

IV. REALIZATION

For the application case, two characteristics are of special interest compared to the numerical examination: increasing the signal strength that can be reaped from the device and ensuring efficient usability and fabrication.

The antenna and detector strip lines would be decoupled. The antenna thickness can then be increased to reduce the current density necessary for excitation and hence Joule heating and increase the lifetime. The detector thickness can be decreased to increase the generated charge-current density. The antenna and detector strip lines do not necessarily need to be colocated any more. The waveguide can have tapered ends to completely suppress wave reflection or optimized length and antenna positions to have suitable reflection at the ends. This would further reduce the necessary current but the strong stray field at the ends may

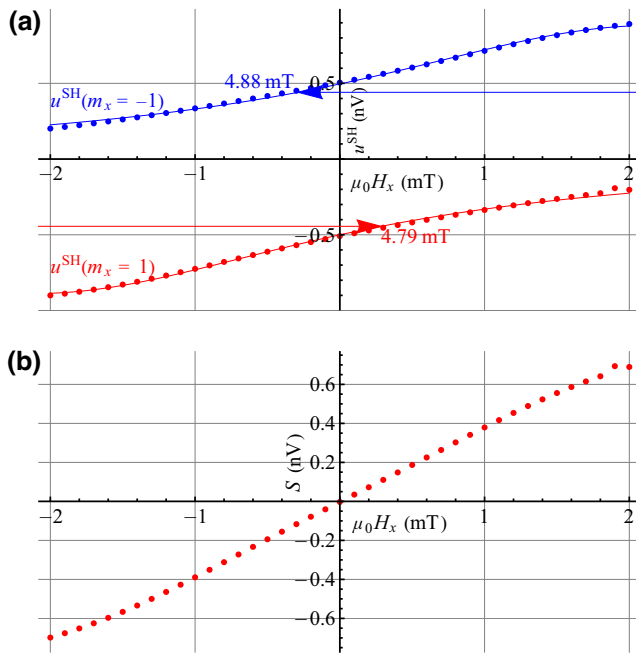


FIG. 8. (a) The sensor voltage signal as a function of the detected field with simulated fabrication errors at 3.3 GHz. The values shown here are calculated as an average over 10 ns of the low-pass-filtered $u^{\text{SH}}(m_x = 1)$ (red) and $u^{\text{SH}}(m_x = -1)$ (blue) with a cutoff at 800 MHz. The data points are computed values and the plotted lines are a fitted Lorentzian, with the line widths noted in the plot. (b) The sensor transfer curve obtained by adding the individual curves from (a) per Eq. (7).

change the reflected behavior of the wave and introduce significant offset.

For a standing wave that is generated via an array of antennas, the free path of a magnon, and therefore the damping of the material, is of limited consequence. This is exacerbated by the additional damping due to spin pumping. Therefore, the employment of a material with ultralow damping does not provide any advantages, especially if it is difficult to fabricate. There then exist two possible variants:

(1) The waveguides can be fabricated from conducting material. This would increase the spin current, and hence the signal, as it is no longer generated by the interaction layer but in the depth of the material on a length scale on the order of λ_{sf} [31]. Having a conducting waveguide would mean that it would short the detector strip lines. To remedy this, instead of the voltage, the charge current can be directly used as the signal and the orthogonal strip lines replaced by ones covering a single waveguide [Fig. 9(a)]. The waveguides can therefore have a reduced cross section, as the relevant dimension is now the length, which should be larger. This also extends the linear regime, hence allowing a higher wave amplitude and signal. The waveguide separation needs to be higher to account for the

detectors. The antenna strip lines have to be separated from the waveguides by a dielectric layer. The patterning of the detector strip lines and vias and the additional dielectric layer, introduce additional complexity. For this variant, a large number of long waveguides increases the signal.

(2) The waveguides can be fabricated from nonconducting material, as in the example analyzed herein. As opposed to the first variant, the spin current is lower, there is no short wiring, the voltage can be collected using orthogonal strip lines, and the waveguides can be shorter but need to have a larger cross section. The waveguide separation can be lower, limited by dipolar coupling. No dielectric layer needs to be inserted. The detector strip lines need to be connected in such a way as to correctly add up the voltages. Figure 9(b) shows the version with simpler structure, where a meandering strip line is employed, with every second strip line raised such that it does not collect a signal. The alternative version, with a more complex but more efficient structure, is not shown here. The strip lines are not connected with each other at the end but by an additional layer of vias above, connecting opposite ends of the strip lines. This would yield a more complex-spiral like structure. For this variant, a large number of crossing points between waveguides and detector strip lines increases the signal.

Although the design analyzed in the computations herein follows the insulator-and-voltage approach, this has been mostly for computational reasons. It would seem that the conductor-and-current approach offers superior performance in application.

Periodical inversion of the magnetization, to provide the two signals for additive measurement, is a challenge in a realized system. It is, at the core, the dilemma of the ease of switching the magnetization versus the stability against off-axis fields. We would like to point out the possibilities of achieving proper inversion using on-chip structures. Elaborate switching schemes will most likely be necessary in this case. Such methods have been explored by others, as the problem is a common one. It is advantageous that detection and antenna lines exist in this device, because those can be employed as support. The whole device would be sandwiched between large strip-line antennas. Pulsed signals in the excitation antennas can nucleate domains [37], which can then be grown by the large field of the antenna. Another possibility to create local domains is through the use of spin-orbit torque, generated by current through the detection lines [38]. Microwave-assisted switching [39] is also a possibility. In any case, the inversion needs to be as complete as possible to minimize hysteresis effects. Tapered waveguides are advantageous to that effect [40]. In the worst case, an off-chip coil will be needed to achieve the desired effect. Such coil-flipping

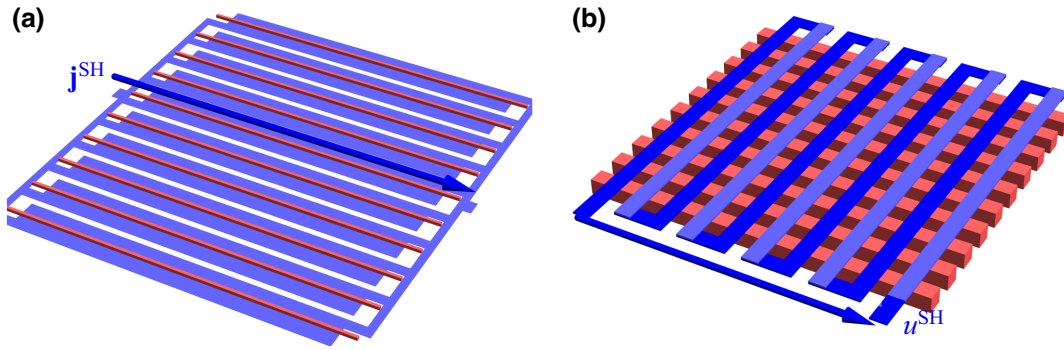


FIG. 9. The proposed realization variants of the concept. The excitation antennas are not shown for clarity. Waveguides are in light red and current-carrying detectors and vias in shades of blue. (a) The variant using the generated current as output signal. (b) The variant using the generated voltage as output signal. Every second strip line of the detector (light blue) is raised such that it does not collect a signal to enable correct addition of signal voltages.

schemes have been used successfully for AMR sensors for more than two decades [41].

V. CONCLUSIONS

The two widespread methods for magnetic field measurements both require special treatment to achieve an offset-free transfer curve. We have presented a field sensor based on a standing spin wave, and its field-dependent shift of the dispersion curve, that can eliminate offset without the need for additional contacts or devices. Micromagnetic analyses have been shown, demonstrating the resulting transfer curve as well as illustrating the peculiarities of the method. The appendixes provide insight into the offset that remains for numerical reasons and the offset that will be introduced by manufacturing deviations.

From a purely physics point, we have shown nanoscale cross-diffusion effects for magnon spin pumping and the resulting ac signal, an effect that is too weak to access in experiments.

In addition, we have proposed various on-chip realizations of our design and provided a qualitative analysis of their strengths and weaknesses. The necessary inversion of the magnetization of the waveguide will be a specific challenge for a working device.

ACKNOWLEDGMENTS

This research was funded in whole, or in part, by the Austrian Science Fund (FWF) I 4917-N “Non-reciprocal 3D architectures for magnonic functionalities.” The computational results presented have been achieved using the Vienna Scientific Cluster (VSC).

APPENDIX A: NUMERICAL ERROR ANALYSIS

As starting point, we refer to Fig. 7(a).

From the symmetry argument, we expect the offset for the zero-field case ($H_x = 0$) to be of equal magnitude, but opposite sign, for the two cases. This, of course, cannot be expected for a numerical computation. The computed voltages u^{SH} are -1.4684 nV and 1.4729 nV (ignoring the small standard deviation of those values). This results in an offset of 4.5 pV or 5 nT. This remaining offset results from several factors:

- (1) There are errors resulting from the numerical computation itself.
- (2) Due to long computation times and time limits on the VSC, the simulation runs had to be divided into smaller segments (three parts for the standing wave to form and two parts for the spin-pumping calculation). Restarting of the numerical integrator introduces a noticeable error at the start of each segment.
- (3) The generated voltage signal was still limited to approximately 15.2 ns, which introduces severe spectral leakage in the Fourier transform and hence makes the low-pass operation not very accurate. Figure 5(b) uses the Fourier transform from a single locally computed signal eight times as long, to minimize leakage.

The way in which the transfer curve is generated is by summing the two individual signals from Fig. 7(a). From the same symmetry argument, we would expect the difference Δu between the two signals to be constant. This is plotted in Fig. 10.

While the sign does not matter, the fact that this is not constant and shows some structure is important. We attribute this structure to numerical errors. We can trace this deviation to the behavior of the precessional motion as a function of the magnetic field. Figure 11 shows the maximum transversal magnetization—in other words, the magnon amplitude—in the waveguide for the two cases. This shape corresponds to the voltage peak of the standing magnon in Fig. 6(b). Since the working point

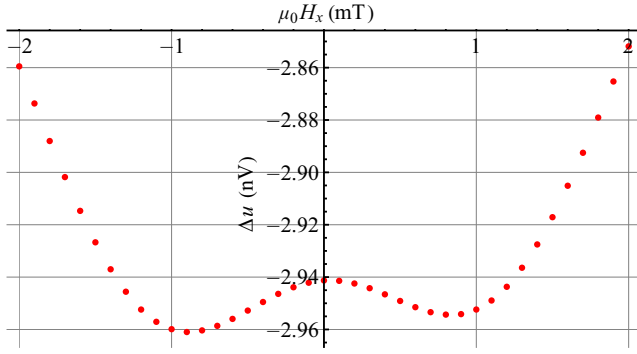


FIG. 10. The sensor voltage difference as a function of the detected field at 3.3 GHz. The values shown here are calculated as an average over 10 ns of the low-pass-filtered u^{SH} with a cutoff at 800 MHz.

is located at the flank of the peak, this gets replicated here.

A larger amplitude also means faster precession (in that dm/dt is larger). We can therefore infer from Fig. 11 that the numerical error of the individual voltages should be larger for higher amplitude, simply due to numerical limits for faster processes. In Fig. 10, the errors of the two signals get combined, resulting in noticeable peaks at roughly the positions where the amplitude, and hence the precession speed, reaches a maximum. This would then also mean that the real Δu should be of lower magnitude than the numerical results.

The fact that the peaks in Fig. 10 are not symmetrical—and also why the offset mentioned above does not vanish—may simply originate from the built-in asymmetry of the finite-element mesh. This would then likely introduce asymmetric numerical errors.

We can also examine the contribution of off-axis fields. In the best case, there would be none and the resulting signal would be identical to the one from only longitudinal

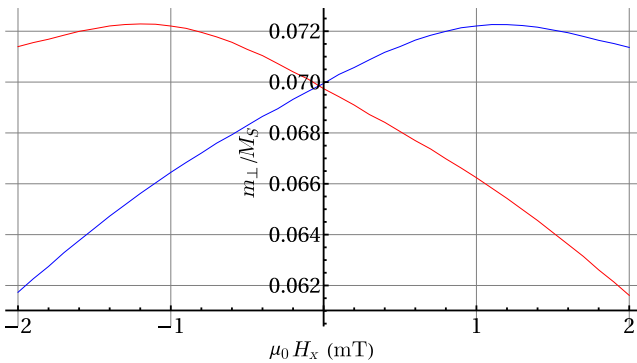


FIG. 11. The maximum magnetization transversal component (the maximum magnon amplitude) in the waveguide as a function of the detected field at 3.3 GHz. $m_x = 1$ (red) and $m_x = -1$ (blue).

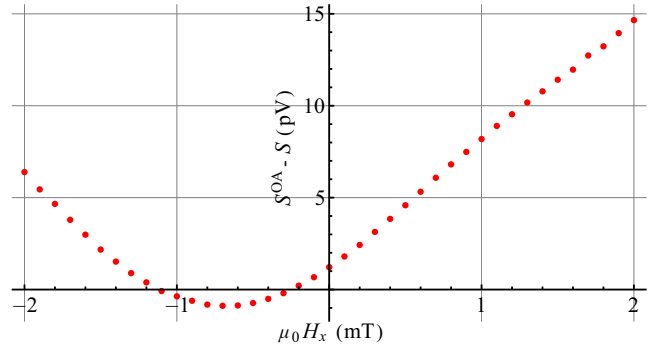


FIG. 12. The sensor signal difference created by off-axis components as a function of the detected field at 3.3 GHz.

fields. The difference is depicted in Fig. 12. What is immediately noticeable is that there is even a difference at zero field, although this is clearly wrong from a physics viewpoint. The difference results from different segmentation of the computations (the consequences of it have been mentioned above): $3 + 2$ for the normal signal and $4 + 4$ for the off-axis case (due to higher computational complexity). Therefore, the error from restarting the integrator is different in both cases and introduces the difference (this difference cannot be expected to be just a constant shift, valid for all fields).

To understand the field-dependent behavior of the difference, we can refer to Fig. 10. The left peak is more pronounced there and hence it is not unexpected that comparison of two such signals amplifies this peak.

APPENDIX B: SIMULATED FABRICATION ERRORS

Table II lists the modified geometrical parameters of the system. It should be noted that this is some kind of worst case.

Again, from the symmetry argument, we would expect the difference Δu between the two signals to be constant.

TABLE II. The modified system dimensions: waveguide width, 50.2829 nm; waveguide height, 48.3336 nm; o is the position offset.

Antenna	$w(\text{nm})$	$h(\text{nm})$	$o(\text{nm})$
1	101.691	11.8031	+2.42
2	98.5148	14.1532	+7.886
3	77.955	14.6202	+0.706
4	75.7064	14.2496	-12.226
5	102.86	14.3876	+11.743
6	89.9662	16.7913	-5.6602
7	81.6407	17.0589	+5.684
8	89.9388	13.9901	+15.15
9	71.6058	12.9165	-13.251
10	89.7372	14.4093	+12.54

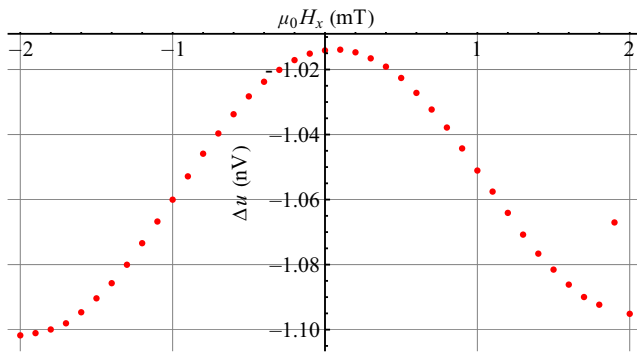


FIG. 13. The sensor voltage difference as a function of the detected field with simulated fabrication errors. The values shown here are calculated as an average over 10 ns of the low-pass-filtered u^{SH} with a cutoff at 800 MHz.

This is plotted in Fig. 13. The structure observable in Fig. 10 is now absent; again, the sign does not matter. It can thus no longer be said that only numerical errors contribute to the remaining signal offset. The symmetry of the system is now notably broken and complete cancellation of the offset can no longer be expected.

- [1] R. C. Jaklevic, J. Lambe, A. H. Silver, and J. E. Mercereau, Quantum interference effects in Josephson tunneling, *Phys. Rev. Lett.* **12**, 159 (1964).
- [2] G. Balasubramanian, P. Neumann, D. Twitchen, M. Markham, R. Kolesov, N. Mizuochi, J. Isoya, J. Achard, J. Beck, J. Tissler, V. Jacques, P. R. Hemmer, F. Jelezko, and J. Wrachtrup, Ultralong spin coherence time in isotopically engineered diamond, *Nat. Mater.* **8**, 383 (2009).
- [3] R. Popovic, *Hall Effect Devices* (CRC Press, Boca Raton, FL, 2003).
- [4] P. Ripka, *Magnetic Sensors and Magnetometers* (Artech House, Norwood, MA, 2021), 2nd ed.
- [5] J.-G. J. Zhu and C. Park, Magnetic tunnel junctions, *Mater. Today* **9**, 36 (2006).
- [6] R. Slatter, in *Micro-Nano-Integration; 7th GMM-Workshop* (VDE, Dortmund, 2018), p. 1. <https://ieeexplore-ieee.org/abstract/document/8580243>.
- [7] H. Weitensfelder, H. Brueckl, A. Satz, K. Pruegl, J. Zimmer, S. Luber, W. Raberg, C. Abert, F. Bruckner, A. Bachleitner-Hofmann, R. Windl, and D. Suess, Comparison of sensitivity and low-frequency noise contributions in giant-magnetoresistive and tunneling-magnetoresistive spin-valve sensors with a vortex-state free layer, *Phys. Rev. Appl.* **10**, 054056 (2018).
- [8] M. Julliere, Tunneling between ferromagnetic films, *Phys. Lett. A* **54**, 225 (1975).
- [9] M. D. Cubells-Beltran, C. Reig, D. R. Munoz, S. I. P. C. de Freitas, and P. J. P. de Freitas, Full Wheatstone bridge spin-valve based sensors for IC currents monitoring, *IEEE Sens. J.* **9**, 1756 (2009).
- [10] R. Ferreira, E. Paz, P. P. Freitas, J. Ribeiro, J. Germano, and L. Sousa, 2-axis magnetometers based on full wheatstone bridges incorporating magnetic tunnel junctions connected in series, *IEEE Trans. Magn.* **48**, 4107 (2012).
- [11] P. Munter, A low-offset spinning-current Hall plate, *Sens. Actuator A Phys.* **22**, 743 (1990).
- [12] M.-A. Paun, J.-M. Sallese, and M. Kayal, Offset and drift analysis of the Hall effect sensors, *Dig. J. Nanomater. Biostruct.* **7**, 883 (2012).
- [13] *CT100 Datasheet*, Crocus Technology (2021), <https://crocus-technology.com/wp-content/uploads/2021/09/CT100-Data-Sheet-Rev2.0.pdf>.
- [14] *CT130 Datasheet*, Crocus Technology (2023), [https://crocus-technology.com/datasheets/CT130 Data Sheet.pdf](https://crocus-technology.com/datasheets/CT130%20Data%20Sheet.pdf).
- [15] S. Takahashi, in *Handbook of Spintronics* (Springer Netherlands, Dordrecht, the Netherlands, 2016), p. 1445.
- [16] M. I. Dyakonov, Magnetoresistance due to edge spin accumulation, *Phys. Rev. Lett.* **99**, 126601 (2007).
- [17] O. Haas, B. Dufay, and S. Saez, Development of a magnonic-based magnetic sensor: Comparison of two different implementations with YIG material, *IEEE Trans. Magn.* **59**, 1 (2023).
- [18] M. Inoue, A. Baryshev, H. Takagi, P. B. Lim, K. Hatafuku, J. Noda, and K. Togo, Investigating the use of magnonic crystals as extremely sensitive magnetic field sensors at room temperature, *Appl. Phys. Lett.* **98**, 132511 (2011).
- [19] P. Talbot, A. Fessant, and J. Gieraltowski, Electromagnetic sensors based on magnonic crystals for applications in the fields of biomedical and NDT, *Procedia Eng.* **120**, 1241 (2015).
- [20] P. J. Metaxas, M. Sushruth, R. A. Begley, J. Ding, R. C. Woodward, I. S. Maksymov, M. Albert, W. Wang, H. Fangohr, A. O. Adeyeye, and M. Kostylev, Sensing magnetic nanoparticles using nano-confined ferromagnetic resonances in a magnonic crystal, *Appl. Phys. Lett.* **106**, 232406 (2015).
- [21] A. Barman, *et al.*, The 2021 magnonics roadmap, *J. Phys.: Condens. Matter* **33**, 413001 (2021).
- [22] A. V. Chumak, *et al.*, Advances in magnetics roadmap on spin-wave computing, *IEEE Trans. Magn.* **58**, 1 (2022).
- [23] P. M. Braganca, B. A. Gurney, B. A. Wilson, J. A. Katine, S. Maat, and J. R. Childress, Nanoscale magnetic field detection using a spin torque oscillator, *Nanotechnology* **21**, 235202 (2010).
- [24] D. Tonini, K. Wu, R. Saha, and J.-P. Wang, Magnetic field detection using spin-torque nano-oscillator combined with magnetic flux concentrator, *AIP Adv.* **13**, 035228 (2023).
- [25] Y. Xu, Y. Yang, Z. Luo, B. Xu, and Y. Wu, Macrospin modeling and experimental study of spin-orbit torque biased magnetic sensors, *J. Appl. Phys.* **122**, 193904 (2017).
- [26] Y. Kajiwara, K. Harii, S. Takahashi, J. Ohe, K. Uchida, M. Mizuguchi, H. Umezawa, H. Kawai, K. Ando, K. Takanashi, S. Maekawa, and E. Saitoh, Transmission of electrical signals by spin-wave interconversion in a magnetic insulator, *Nature* **464**, 262 (2010).
- [27] C. W. Sandweg, Y. Kajiwara, A. V. Chumak, A. A. Serga, V. I. Vasyuchka, M. B. Jungfleisch, E. Saitoh, and B. Hillebrands, Spin pumping by parametrically excited exchange magnons, *Phys. Rev. Lett.* **106**, 216601 (2011).
- [28] A. V. Chumak, A. A. Serga, M. B. Jungfleisch, R. Neb, D. A. Bozhko, V. S. Tiberkevich, and B. Hillebrands, Direct

- detection of magnon spin transport by the inverse spin Hall effect, *Appl. Phys. Lett.* **100**, 082405 (2012).
- [29] A. G. Gurevich and G. A. Melkov, *Magnetization Oscillations and Waves* (CRC Press, Boca Raton, Florida, 1996).
- [30] E. V. Skorohodov, R. V. Gorev, R. R. Yakubov, E. S. Demidov, Yu.V. Khivintsev, Yu.A. Filimonov, and V. L. Mironov, Ferromagnetic resonance in submicron permalloy stripes, *J. Magn. Magn. Mater.* **424**, 118 (2017).
- [31] M. Gattringer, C. Abert, F. Bruckner, A. Chumak, and D. Suess, Micromagnetically integrated numerical model of spin pumping based on spin diffusion, *Phys. Rev. B* **106**, 024417 (2022).
- [32] D. Suess, A. Bachleitner-Hofmann, A. Satz, H. Weitensfelder, C. Vogler, F. Bruckner, C. Abert, K. Prügl, J. Zimmer, C. Huber, S. Luber, W. Raberg, T. Schrefl, and H. Brückl, Topologically protected vortex structures for low-noise magnetic sensors with high linear range, *Nat. Electron.* **1**, 362 (2018).
- [33] C. Abert, L. Exl, F. Bruckner, A. Drews, and D. Suess, MAGNUM.FE: A micromagnetic finite-element simulation code based on FEniCS, *J. Magn. Magn. Mater.* **345**, 29 (2013).
- [34] Y. Sun, H. Chang, M. Kabatek, Y.-Y. Song, Z. Wang, M. Jantz, W. Schneider, M. Wu, E. Montoya, B. Kardasz, B. Heinrich, S. G. E. te Velthuis, H. Schultheiss, and A. Hoffmann, Damping in yttrium iron garnet nanoscale films capped by platinum, *Phys. Rev. Lett.* **111**, 106601 (2013).
- [35] F. Bruckner, M. d'Aquino, C. Serpico, C. Abert, C. Vogler, and D. Suess, Large scale finite-element simulation of micromagnetic thermal noise, *J. Magn. Magn. Mater.* **475**, 408 (2019).
- [36] K. Ando, S. Takahashi, J. Ieda, Y. Kajiwara, H. Nakayama, T. Yoshino, K. Harii, Y. Fujikawa, M. Matsuo, S. Maekawa, and E. Saitoh, Inverse spin-Hall effect induced by spin pumping in metallic system, *J. Appl. Phys.* **109**, 103913 (2011).
- [37] O. Alejos, V. Raposo, L. Sanchez-Tejerina, and E. Martinez, Efficient and controlled domain wall nucleation for magnetic shift registers, *Sci. Rep.* **7**, 11909 (2017).
- [38] Z. Ren, S. Liu, L. Jin, T. Wen, Y. Liao, X. Tang, H. Zhang, and Z. Zhong, Reconfigurable nanoscale spin-wave directional coupler using spin-orbit torque, *Sci. Rep.* **9**, 7093 (2019).
- [39] X. Fan, Y. S. Gui, A. Wirthmann, G. Williams, D. Xue, and C.-M. Hu, Electrical detection of microwave assisted magnetization switching in a permalloy microstrip, *Appl. Phys. Lett.* **95**, 062511 (2009).
- [40] D. Kuźma, Ł. Laskowski, J. W. Kłos, and P. Zieliński, Effects of shape on magnetization switching in systems of magnetic elongated nanoparticles, *J. Magn. Magn. Mater.* **545**, 168685 (2022).
- [41] P. Ripka, M. Tondra, J. Stokes, and R. Beech, AC-driven AMR and GMR magnetoresistors, *Sens. Actuator A Phys.* **76**, 225 (1999).